SCIENCE CHINA
Chemistry

•ARTICLES•

September 2025 Vol.68 No.9: 4459–4467
https://doi.org/10.1007/s11426-024-2544-y

Gas-phase synthesis and soft-landing deposition of imidazole clusters with narrowband emission

Qiuhao Yi[1,2], Siyang Ye[3], Haiming Wu[1†], Yuxi Tian[3*] & Zhixun Luo[1,2*]

[1]*Beijing National Laboratory for Molecular Sciences (BNLMS), State Key Laboratory for Structural Chemistry of Unstable and Stable Species, Institute of Chemistry, Chinese Academy of Sciences, Beijing 100190, China*
[2]*School of Chemical Sciences, University of Chinese Academy of Sciences, Beijing 100049, China*
[3]*School of Chemistry and Chemical Engineering, Nanjing University, Nanjing 210023, China*

Received December 22, 2024; accepted January 20, 2025; published online March 19, 2025

Imidazole and its derivatives are common in bioactive molecules and function as pharmacophores in diverse medications. This study examines the gas-phase reactions of imidazole and benzylimidazole using a self-developed reflectron time-of-flight mass spectrometer equipped with dual sources and a downstream tube reactor. It was found that the Cu^+/Ag^+ ions readily coordinate with these organic molecules to create metal complexes; furthermore, the plasma-assisted Cu^+/Ag^+ ions enable C–N coupling reactions to generate a $C_{17}H_{17}N_2^{+\bullet}$ radical assigned to 1,3-dibenzylimidazole, along with hydropolymerization to form molecular clusters through hydrogen bond linkers. With Im_3H^+ as a representative, we attained soft-landing deposition and measured its fluorescence. Interestingly, the deposited quantum dots of Im_3H^+ clusters exhibit narrow-width emission at 516 nm, which fits well with the time-dependent density functional theory (TD-DFT) calculation results. Through DFT calculations, we also elucidated the chemical interactions in these cluster systems. This study advances the basic understanding of heteroaromatic compounds and their weakly bound clusters, and provides a solvent-free synthesis technique for organic molecular clusters and metal-organic complexes.

imidazole clusters, narrowband emission, soft-landing deposition, metal-organic complex, mass spectrometry

Citation: Yi Q, Ye S, Wu H, Tian Y, Luo Z. Gas-phase synthesis and soft-landing deposition of imidazole clusters with narrowband emission. *Sci China Chem*, 2025, 68: 4459–4467, https://doi.org/10.1007/s11426-024-2544-y

1 Introduction

Imidazole ($C_3H_4N_2$, abbreviated as "Im") is common in epoxy resins, as a curing agent to improve electrical insulation and mechanical properties. The molecular structure of imidazole is a five-membered heteroaromatic diazole ring with two nitrogen atoms at positions one and three. The 1-position nitrogen atom is an imino group (–NH–) with a lone pair of valence electrons that promotes ring conjugation, lowering electron density on the N atom and causing inadvertent N–H activation. The 3-position (–N=) nitrogen atom favors the ligand coordination or alkylation reactions. In view of this unique structure, imidazole exhibits both acidic and basic properties, underscoring its significance in the synthesis of pyridine, pyrrole, and diverse metal complexes [1,2]. Imidazole and its derivatives also function as active mediums for proton transport in molecular networks [3,4], and present interesting alternatives in fluorescence sensing [5,6]. Among the imidazole derivatives, benzylimidazole ($C_{10}H_{10}N_2$, abbreviated as "bim") and metal-imidazole complexes have attracted considerable research interest [7,8], being employed in many medications and serving crucial functions in diverse natural products and biological

†Present address: Department of Chemistry, Tsinghua University, Beijing 100084, China.
*Corresponding authors (email: tyx@nju.edu.cn; zxluo@iccas.ac.cn)

systems [9–11] Meanwhile, small aggregates or hydrogen-bonded clusters of such heteroaromatic molecules provide a valuable means to comprehend the structure-property relationships of materials and the weak intermolecular interactions inside biosystems [12]. However, there is still little comprehension of the mechanisms governing molecular clusters in similar contexts.

Gas-phase reactions are crucial in various scientific fields, offering insights into the fundamental thermodynamics and kinetics of chemical processes [13]. Molecules and clusters in the gas phase exhibit high mobility and kinetic energy, facilitating effective collisions between reactants and resulting in potentially faster reaction rates compared to solid or liquid phases [14]. Also, gas-phase reactions can be studied under controlled conditions, simplifying calculations related to enthalpy changes and reaction rates. Due to the sensitivity to gas pressure and temperature, both reaction rates and equilibria, as well as product selectivity, can be finely adjusted. Furthermore, soft-landing deposition of gas-phase reaction products facilitates the comprehension of size-dependent reactivity and the atomic-level link between surface structures and properties [15–29].

This study examined the gas-phase interactions of Cu^+/Ag^+ cations with imidazole and benzylimidazole utilizing a custom-built reflectron time-of-flight mass spectrometer (Re-TOFMS) with a compact reaction tube and dual sources (Figure S1, Supporting Information online), i.e., magnetron sputtering (MagS) and thermal evaporation (TVa) sources. Consequently, a series of Cu^+/Ag^+ complexes coordinated with one or two Im/bim molecules were formed at a lower evaporation temperature of about 40 °C, whereas protonated molecular clusters $(Im)_nH^+$ (n = 2–4) were detected at higher temperatures up to 60 °C. The structures and intramolecular interactions of these metal complexes and molecular clusters were further examined by density functional theory (DFT) calculations, demonstrating tunable metal-imidazole coordination and hydrogen-bond interactions linked to their selective reactions. Furthermore, we accomplished soft-landing deposition for a weakly-bonded molecular cluster, $(Im)_3H^+$, and measured its fluorescence. The narrow-band emission at 516 nm aligns closely with the results of the time dependent (TD)-DFT calculations.

2 Experimental

2.1 Cluster generation

The experiments were performed in a homemade reflection time-of-flight mass spectrometry (Re-TOF-MS) instrument, which is equipped with a magnetron sputtering (MagS) ion source and a fixed tube reactor [30]. The MagS source was used to generate Cu and Ag cation, and installed in the front of the whole apparatus. A copper or silver disk (Ø = 50.8 mm, and 4–5 mm thickness, 99.99% purity) was fixed to the magnetron head and served as the sputtering target material. The working gas Ar was brought into the chamber by a mass flowmeter (Alicat Scientific, Inc.). A DC power supply (3 kW, Kurt J. Lesker) was used to provide the high voltage for the MagS source. Under the DC electric field, the ionized Ar cations bombarded the target and the metal atoms and small clusters were sputtered out and carried by He buffer gas out of the nozzle of the MagS source.

2.2 Metal-organic reaction

A tube reactor was designed downstream of the MagS source and combined with a thermal vaporization (TVa) source beneath the reactor in the vertical direction (Figure S1). Solid samples of the organic chemicals were held in a stainless-steel crucible which can be heated up to 300 °C under precise temperature control. The gaseous organic molecules will go upwards into the tube reactor through a mini skimmer and interact with the horizontal molecule beam, leading to metal-organic chemical reactions. A high-vacuum plasma cleaning setup (XEI Evactron EP) was employed to clean the vacuum chamber after each experiment to avoid interference caused by residual contamination. In the TOF chamber, a vacuum differential is achieved by a vacuum pumping setup and a normal skimmer (Ø = 2.5 mm).

2.3 Soft-landing deposition

Following the gas-phase reactions, soft-landing deposition of mass-selected $(Im)_3H^+$ clusters was dispersed on polymethyl methacrylate (PMMA)-coated cover glass. The PMMA films were coated on the cover glass by spin-coating method, which was then installed with a copper foil having a 3 mm diameter aperture in the centre. The exposed area of the copper foil coupled with PMMA-coated cover glass as the deposition target, with its centre aligned coaxially to the cluster beam. Repulsive voltages were supplied to the copper foil substrate to reduce the kinetic energies of the target cluster ions, along with tuneable voltages on the focus lens and deflection electrodes, resulting in improved deposition efficiencies of the mass-selected clusters. A sampling repetition frequency at 4000 Hz was used for the soft-landing deposition, lasting for 2 h.

2.4 Fluorescence measurement

All optical kinetics and spectra were measured on a home-built wide-field microscope organized around an inverted microscope (Olympus IX73). A supercontinuum pulsed laser (440–460 nm, Fianium) was used as the light source after passing through a 450-nm laser-line filter (FB450-10, THORLABS). The fluorescent signal was collected by an oil

objective lens (Olympus LUCPlanFI 60×, numerical aperture NA = 1.25) and recorded by an sCMOS camera (Dhyana 95, Fujian Tucsen electrooptics Co., Ltd) after passing through a 473 nm long-pass filter (BLPO1-473R-25, Semerock).

2.5 Computational

The optimization, frequency, and energy calculations were carried out using DFT within the Gaussian 16 software package [31]. The geometric structures of reactants and products were fully optimized at B3LYP/6-311++G(d,p) level. We employed Molclus code, combined with the software Molecular Orbital Package (MOPAC 2016™) [32], to search for possible conformations of the metal-organic complexes and the Im/bim molecular clusters [33]. Further calculations on the low-lying structures of the molecular clusters were carried out using the same method with a mixed basis set, namely, PBE0-D3 in conjunction with SDD (Stuttgart-Dresden) and 6-311+G(d,p) for the metallic (Cu^+, Ag^+) and non-metallic (C, H, N) atoms respectively [34]. The frequency calculations were performed to ensure that the clusters observed in the mass spectra have zero imaginary frequency. All the energies were calculated with zero-point corrections. Potential energy scanning, frontier orbital, natural bond orbital (NBO) analysis and charge population analysis were performed for further investigations [35]. Energy decomposition analysis (EDA) was conducted using the Amsterdam density functional (ADF 2021) program package at the PBE-D3(BJ)/TZP level [36–38]. Electrostatic potential, Hirshfeld atomic charge distribution and the sign $(\lambda_2)\rho$ coloured δg^{inter} isosurface maps using the independent gradient model based on Hirshfeld partition (IGMH) of molecular density were calculated and analysed with the help of Multiwfn software [39,40]. The structures and orbital patterns were plotted by using visual molecular dynamics (VMD) [41,42] software.

The ground state S_0 and the first excited state S_1 were optimized in TD-DFT calculations, with Grimme's D3 correction [43], using BP86 functional [44] and def2-TZVP basis set [45]. A three-step procedure was used to calculate the fluorescence spectra. First, the S_0 geometry of a molecule or cluster was optimized; second, the S_1 geometries were optimized based on the optimized S_0 structures, where the lengths of N–H hydrogen bonds in the cluster were restricted to maintain its framework; third, based on results of the frequency calculation at S_0 and S_1, the calculation of Franck-Condon integral was conducted to obtain the deexcitation transition and fluorescence spectra. To simulate a spectral profile as the experiment, the stick-spectrum was broadened using a Gaussian function with an appropriate full width at half maximum (FWHM) via Multiwfn software [42], specifically, 0.10 eV for the protonated imidazole cluster $(Im)_3H^+$.

3 Results and discussion

Figure 1 presents the mass spectra of Cu^+ and Ag^+ ions produced by the MagS source before and after reacting with imidazole and 1-benzylimidazole respectively. Both copper and silver have isotope distributions (Figure 1A, B), which is beneficial to the mass peak assignment (details in Figures S2 and S3). Interestingly, the molecular ion ($Im^{+\bullet}$) is transcended by its hydrogenation peak (ImH^+, i.e., $C_3H_5N_2^+$) which dominates the mass spectra (Figure 1C, D). It is inferred that the neutral imidazole could be readily ionized and protonated with the help of energetic Ar^+ and Cu^+/Ag^+ ions. As mentioned above, the 3-position nitrogen atom (–N=) of imidazole has a relatively dense electron cloud, which favours the interaction with a free proton (H^+) via nucleophilic attack to form ImH^+. In addition to this product, Cu^+ and Ag^+ readily react with imidazole to produce metal complexes, i.e., $[Cu(Im)_{1,2}]^+$ and $[Ag(Im)_{1,2}]^+$.

We have also studied the reactions of Cu^+ and Ag^+ ions with an imidazole derivate, 1-benzylimidazole ($C_{10}H_{10}N_2$), of which a benzyl group replaces the hydrogen atom on the 1-position N atom of the imidazole ring. The results of mass spectrometric experiments conducted at comparable conditions are shown in Figure 1E, F. Interestingly, the strongest mass peak does not correspond to the molecular ion or its protonated product; instead, a dissociative fragment $C_7H_7^{+\bullet}$ emerges, which is often seen in the organic mass spectrometry due to the fragmentation of molecules containing the benzyl units. This is also accompanied by a secondary reaction product $C_{17}H_{17}N_2^{+\bullet}$ assigned to 1,3-dibenzylimidazole, suggesting a breakage of the C–N bond and recombination with a benzylimidazole molecule (namely, $C_7H_7^{+\bullet}$ + bim → $C_{17}H_{17}N_2^{+\bullet}$). Metal complexes of $[Cu(bim)_{1,2}]^+$ and $[Ag(bim)_{1,2}]^+$ are also observed as products, indicating that Cu^+/Ag^+ could coordinate with the unsaturated 3-position N atom on the imidazole ring without being affected by the benzyl group on the other side. The interactions between the metal and molecules cause electron transfer and ligand coordination [46], which weakens the C–N bond and makes it easier for adduct-reaction products to grow.

Considering that imidazole and benzylimidazole have different melting points, we tried the experiments under different reaction conditions. Interestingly, when increasing the temperature of the TVa source, the concentration of imidazole vapour rises but the products of $[Cu(Im)_{1,2}]^+$ and $[Ag(Im)_{1,2}]^+$ complexes disappear; instead, a series of molecular clusters $(Im)_{1-4}H^+$ emerge in the mass spectra, as shown in Figure 2A, B. It is supposed that a higher concentration of imidazole monomer from the TVa source could inhibit the coordination of Cu^+/Ag^+ ions, rendering altered reactions in the flow tube reactor. Notably, an impressive previous study also synthesized a minor quantity of such

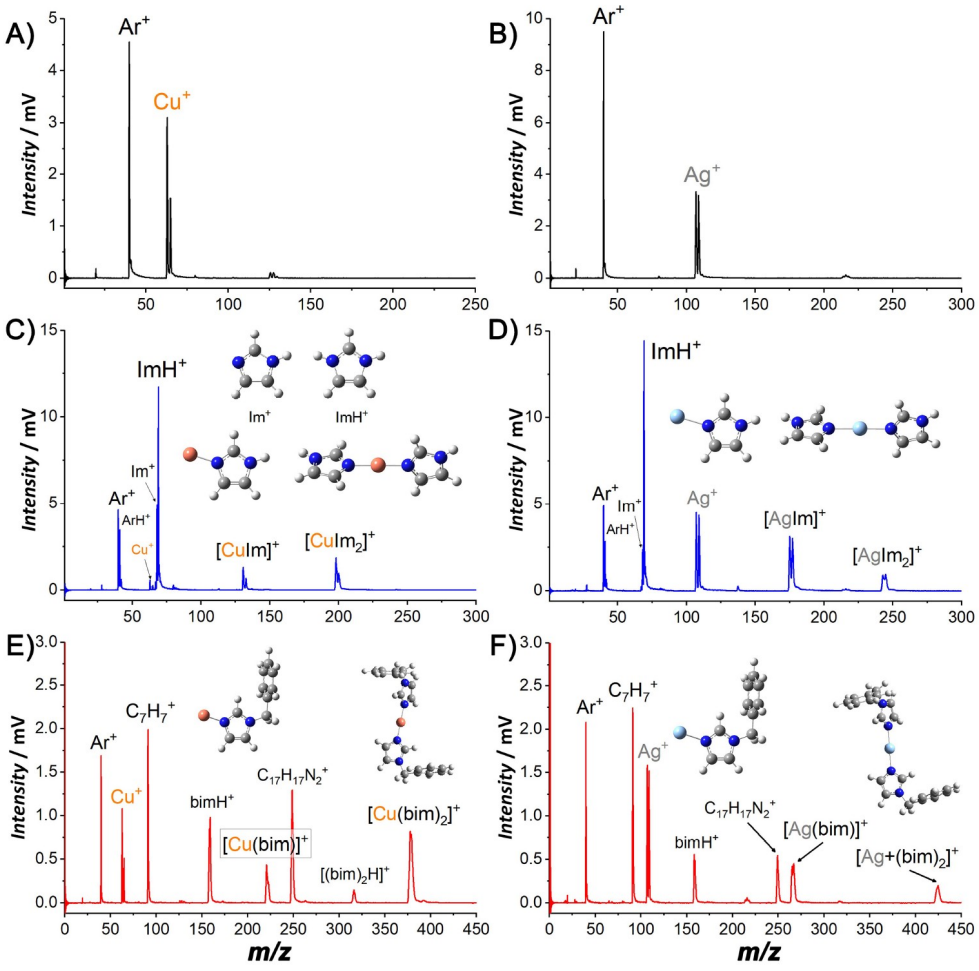

Figure 1 (Color online) Mass spectra of Cu^+ and Ag^+ ions produced by the MagS source (A, B), after reacting with the vapours of imidazole (C, D) and 1-benzylimidazole (E, F) generated by the TVa source, respectively. Relatively lower concentrations were used by controlling the evaporating temperature of the TVa source at ~40 °C. Details see the Supporting Information online.

protonated imidazole clusters $(Im)_{1-3}H^+Ar_x$ by entrainment of imidazole into an Ar-tagged H_3^+ molecular beam, and discussed the structures of $(Im)H^+Ar$, $(Im)_2H^+Ar$, and $(Im)_3H^+Ar$ by infrared predissociation technique, illustrating the important N–H bonding and adjustable intracluster interactions in such systems [47]. A similar phenomenon was also observed in the experiments with benzylimidazole in place of imidazole (Figure 2C, D). Nonetheless, in addition to the protonated clusters $(bim)_{1,2}H^+$, there is a $C_7H_7^+$ fragment due to homolytic cleavage of the C–N bond between the benzyl group and imidazole ring; also, a remarkable mass peak of $C_{17}H_{17}N_2^{+\bullet}$ was observed again, showing the gas-phase synthesis of a new compound, 1,3-dibenzylimidazole ($C_{17}H_{17}N_2^{+\bullet}$) [48]. DFT calculations find a tuning-fork structure for the 1,3-dibenzylimidazole pertaining to dual N–C bond formation in this process [49–51].

Utilizing DFT calculations, we performed further analysis on these imidazole and bim complexes. Figure 3A shows the energy levels of the highest occupied molecular orbitals (HOMO) and lowest unoccupied molecular orbitals (LUMO) based on the DFT-optimized lowest-energy structures (for details see Figures S4–S7), in a comparison with that of the Cu^+/Ag^+ ions and the nascent Im/bim molecules. Notably, the HOMO-LUMO gaps of the di-coordinated complexes, $[Cu(Im)_2]^+$, $[Ag(Im)_2]^+$, $[Cu(bim)_2]^+$ and $[Ag(bim)_2]^+$, are larger than that of the mono-coordinated $[Cu(Im)]^+$, $[Ag(Im)]^+$, $[Cu(bim)]^+$ and $[Ag(bim)]^+$ respectively. We also conducted NBO analysis (inset of Figure 3A) and found that the dominant donor-acceptor interactions ($LP_N \rightarrow LP^*_{Cu/Ag}$) are larger for the di-coordinated complexes. This agrees with their relative stability and is beneficial to the formation of di-coordinated complexes. Interestingly, the HOMOs of these imidazole and benzylimidazole complexes are mainly contributed by the ligand, while the LUMOs are dominated by Cu^+/Ag^+ (Figure 3B), indicative of ligand-to-metal charge transfer interactions. Also, the density of states (DOS) of these complexes exhibit blue shifts compared to the molecule itself (Figures S9–S11), showing reasonable charge-transfer interactions of the lone-pair electrons of the N atom with the unoccupied orbital of the metal.

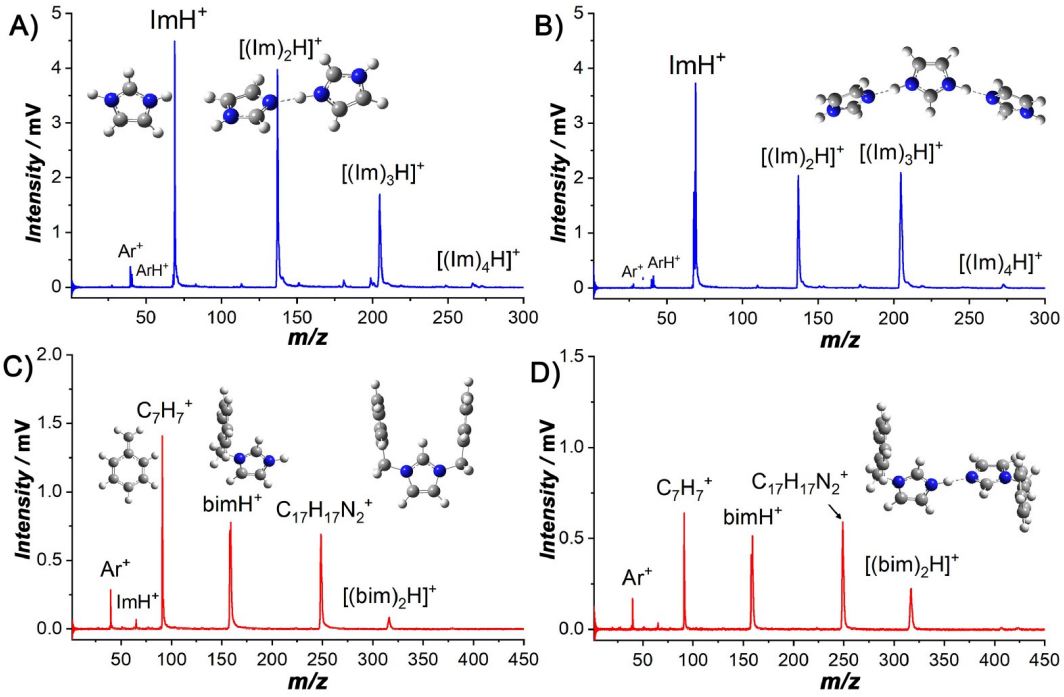

Figure 2 (Color online) (A, B) Mass spectra of the molecular clusters $(Im)_{1-4}H^+$ formed by thermal evaporation of imidazole powder sample in the presence of Cu^+ and Ag^+ ions generated by a MagS source. (C, D) Mass spectra of the molecular clusters $(bim)_{1-2}H^+$, along with a $C_7H_7^{+\bullet}$ fragment and a $C_{17}H_{17}N_2^{+\bullet}$ product, formed by thermal evaporation of benzylimidazole powder sample (~60 °C) in the presence of Cu^+ or Ag^+ ions.

Based on the optimized structures, we also calculated the metal-ligand binding energies in these complexes. It is found that the formation of all these complexes is exothermic, and the energy gain of ligand adsorption becomes smaller at the addition of more Im/bim molecules (Table S1, Supporting Information online). DFT calculations show that the third imidazole molecule is significantly less exothermic, and the distances between Cu/Ag and N atoms in the $[Cu/Ag(Im)_3]^+$ and $[Cu/Ag(bim)_3]^+$ complexes are enlarged, suggesting weakened ligand-metal interactions. This could be the reason why the metal complexes with tri-ligands and tetra-ligands were not observed in the mass spectrometric experiments. In addition, the binding energy of benzylimidazole complexes is slightly higher than that of the imidazole analogues, likely due to the branching aromatic benzene ring that disperses the positive charge. For these metal complexes, topology analysis in the atom-in-molecule (AIM) theory (Table S3) suggests that metal-ligand interactions correspond to non-covalent bonds by noting the positive values of the Laplacian of electron density $\nabla^2\rho$ at the bond critical points (BCPs). Furthermore, we performed EDA for these complexes by dividing the total bonding energy into four components, namely, electrostatic interaction, orbital interaction, Pauli repulsion, and dispersion (Table S2 and Figure S8). As a result, the electrostatic interactions appear as one of the dominant contributions. Meanwhile, orbital interactions exhibit reasonable contributions, but the Pauli repulsion shows comparable values against the bonding, with the dispersion energy being neglectable.

Apart from these complexes, several protonated molecular clusters were also observed under similar conditions (Figure 2). These protonated imidazole and benzylimidazole clusters could be generated via a successive two-step reaction pathway, namely,

$$Cu^+ / Ag^+ + Im / bim \rightarrow Cu / Ag + Im^{+\bullet} / bim^{+\bullet} \quad (1)$$

$$Im^{+\bullet} / bim^{+\bullet} + Im / bim \rightarrow ImH^+ / bimH^+ + [Im-H]^\bullet / [bim-H]^\bullet \quad (2)$$

The first step is essentially associated with a charge-transfer reaction, or referred to as the charge-transfer chemical ionization process [52]. Considering that the calculated first ionization energy of Ar (15.76 eV) is much larger than that of imidazole (8.74 eV) and benzylimidazole (8.17 eV), the chemical ionization by charge exchange with Ar^+ or plasma-assisted Cu^+/Ag^+ ions could be attained efficiently. This is also consistent with the experimental results that the mass peak intensity of Ar^+ and Cu^+/Ag^+ ions decreased with the increasing abundance of $Im^{+\bullet}$ and related products in the mass spectra. Interestingly, the cationic radical $Im^{+\bullet}$ and $bim^{+\bullet}$ react with another molecule or a fragment to form a product of 1,3-dibenzylimidazole (e.g., $bim^{+\bullet} + C_7H_7 \rightarrow C_{17}H_{17}N_2^+$).

With an emphasis on the formation of $(Im)_nH^+$ (n = 2–4), we provide further insights into the protonated organic

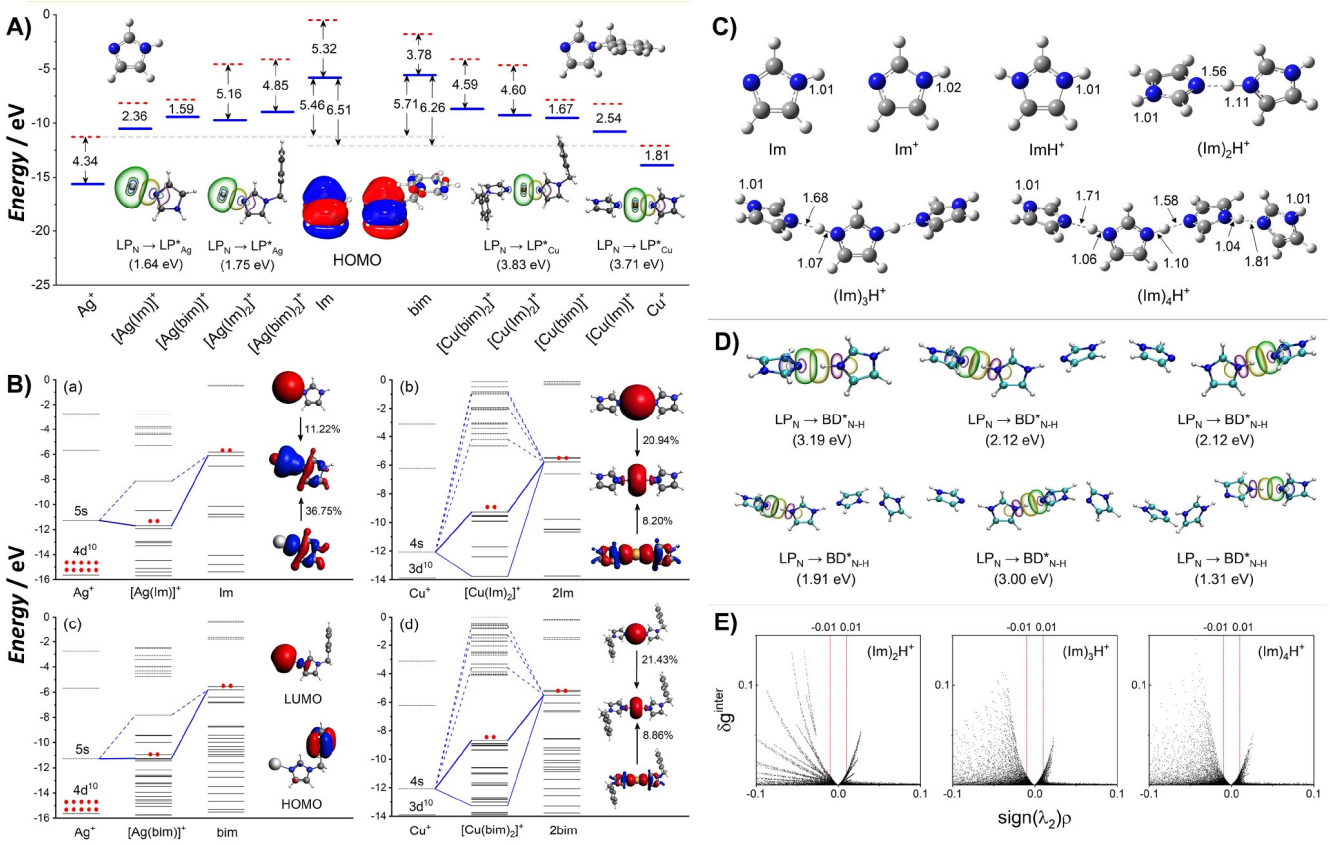

Figure 3 (Color online) (A) Energy level diagrams of the $[M(Im)_{1-2}]^+$ and $[M(bim)_{1-2}]^+$ (M = Cu, Ag) complexes based on their highest occupied molecular orbitals (HOMOs) and lowest unoccupied molecular orbitals (LUMOs). Insets show the dominant natural bond orbital (NBO) interactions and HOMO patterns of the imidazole and benzylimidazole molecules respectively. (B) Kohn-Sham MO energy-level correlation diagram of the four complexes: $[Ag(Im)]^+$ (a), $[Cu(Im)_2]^+$ (b), $[Ag(bim)]^+$ (c), and $[Cu(bim)_2]^+$ (d), calculated by using ADF software. Strong interactions between Cu^+/Ag^+ and Im/bim are coloured in blue lines, with corresponding structures and orbitals displayed on the right. (C) Optimized structures of imidazole molecule, imidazole cation ($Im^{\cdot+}$), protonated imidazole cation (ImH^+) and protonated imidazole clusters $(Im)_nH^+$ (n = 2–4). The distances between N and H atoms are labelled next to them with the unit Å omitted. (D) NBO analysis of protonated imidazole clusters $(Im)_nH^+$ (n = 2–4). LP and LP* refer to occupied and unoccupied antibonding orbital of lone pair electrons, and BD* refers to the diatomic anti-bonding molecular orbitals. Donor and acceptor orbitals are plotted in purple/yellow and blue/green; and the atoms in cyan, blue and white refer to C, N and H, respectively. (E) Two-dimensional (2D) independent gradient model (IGM) scatter plots of δg^{inter} versus sign(λ_2)ρ for protonated imidazole clusters $(Im)_nH^+$ (n = 2–4) at a range $-0.1 \leqslant \text{sign}(\lambda_2)\rho \leqslant 0.1$.

clusters. The increasing product ImH^+ and excessive neutral imidazole promote the subsequent reaction to form a series of protonated imidazole clusters, which can be written as follows:

$$ImH^+ + Im \rightarrow (Im)_2H^+, \quad \Delta E = -1.20 \text{ eV} \tag{3}$$

$$(Im)_2H^+ + Im \rightarrow (Im)_3H^+, \quad \Delta E = -0.92 \text{ eV} \tag{4}$$

$$(Im)_3H^+ + Im \rightarrow (Im)_4H^+, \quad \Delta E = -0.67 \text{ eV} \tag{5}$$

As seen from the above equations, the formation of $(Im)_nH^+$ (n = 2–4) is exothermic, and the energy gain progressively decreases with an increasing number of imidazole molecules. On this basis, the growth for larger molecular clusters (n > 4) would release less energy. Notably, for a usual flow tube reactor, a value of thermal dissociation threshold could be up to 0.4–0.6 eV according to previous literature [53,54]. Therefore, the formation of even larger $(Im)_nH^+$ could suffer from competitive dissociation. This is consistent with the experimental observation of such clusters limited to $(Im)_4H^+$ as mentioned above.

Figure 3C depicts the optimized structures of protonated imidazole clusters $(Im)_nH^+$ (n = 2–4). For neutral Im, cationic Im^+ and ImH^+, the N–H bond lengths are almost the same (~1.10 Å); but for $(Im)_2H^+$, an intermolecular NH···N hydrogen bond is formed with a bond length of 1.56 Å, which is comparable to an intermolecular H···F bond (1.87 Å) [55]. The intermolecular hydrogen bond shortens the original N–H bond of ImH^+ (from 1.10 to 1.01 Å). For $(Im)_3H^+$, it has a highly symmetric structure with two imidazole molecules interacting with the NH on the 1-position and 3-position of ImH^+ from both sides, allowing two hydrogen bonds to be elongated to 1.68 Å. The subsequent $(Im)_4H^+$ continues the chain structure with the third imidazole molecule linked on the NH terminal group of $(Im)_3H^+$, giving rise to weakened hydrogen bonds (1.81, 1.71, and 1.58 Å, respectively). NBO analysis (Figure 3D) shows that the largest intermolecular

interaction belongs to $LP_N \rightarrow BD^*_{N-H}$, corresponding to donor-acceptor orbital overlap interactions between the lone-pair electrons on the N atom and the anti-bonding orbital of N–H in imidazole (details in Figures S12–S14). Again, the overlap interaction between LP_N and BD^*_{N-H} is maximized for $(Im)_2H^+$ (up to 3.19 eV), but weakens for $(Im)_{3,4}H^+$ (2.12 and 1.91 eV). Figure 3E presents further visualized information about the intermolecular interactions by using the independent gradient model (IGM) of topological AIM analysis. The small pinnacles observed at a range of $-0.01 \leqslant \text{sign}(\lambda_2)\rho \leqslant 0.01$ (with red dash line border) correspond to weak Van der Waals interactions, while the large peaks shown in the range of $-0.1 \leqslant \text{sign}(\lambda_2)\rho \leqslant -0.01$ indicate strong hydrogen-bond interactions. For all these $(Im)_nH^+$ clusters, there are no obvious peaks at the weak interaction regions; instead, the IGM scatter plots display large peaks at strong interaction regions assigned to traditional hydrogen bonding interactions, which agrees with the analysis above.

Having elucidated the structural features of these clusters, we then attained soft-landing deposition of the mass-selected $(Im)_3H^+$ clusters, as a representative, on PMMA-coated cover glass. The emphasis on $(Im)_3H^+$ is motivated by the weak intermolecular interactions and its novel chain structure. Figure 4A shows a sketch of the mass selection and cluster deposition strategy. Apart from the five-electrode acceleration, two sets of deflection electrodes were situated downstream of the focus lens, and the cluster ions were regulated by a time-sequence system that allowed the target ions to travel horizontally while deflecting the other ions (Figure 4B). The PMMA films were coated on the cover glass which was then covered with a copper foil having a 3 mm diameter aperture in the centre. The exposed area of the substrate functions as the deposition target, with its centre aligned coaxially with the cluster beam and proper repulsive voltages supplied to the copper foil for soft-landing deposition [56].

For the soft-landing deposition sample of mass-selected $(Im)_3H^+$ clusters, we conducted a fluorescence spectroscopic study. Figure 4C, D show the fluorescence photographs of the PMMA films before and after deposition of the $(Im)_3H^+$ clusters. Fluorescent quantum dots of such clusters can be seen from the fluorescence images. This single-molecule spectroscopic setup has high sensitivity [57], enabling us to collect fluorescent spectra and kinetics of such soft-landed clusters. A typical spectrum and the fluorescence intensity trace are given in Figure 4E, F. The fluorescence spectrum of the $(Im)_3H^+$ clusters shows two distinctive peaks at 516 and 686 nm respectively (an additional waist-peak at 478 nm is likely due to the 473-nm long-pass filter). Under the high-intensity laser irradiation of 5 mW, the clusters show a rapid photobleaching process. Notably, the simulated fluorescence spectrum of $(Im)_3H^+$ based on TD-DFT calculations also exhibits a dominant emission peak at 516 nm, corresponding

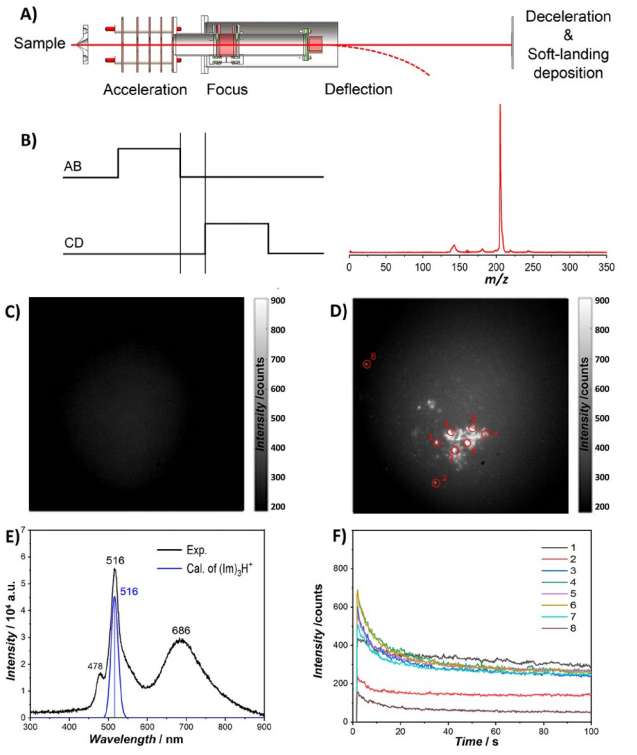

Figure 4 (Color online) (A) A sketch of the mass selection and cluster deposition strategy. (B) Time sequence for precise mass selection, allowing the target cluster ions $(Im)_3H^+$ to travel horizontally while deflecting the other ions before and after the preset time-of-flight. (C, D) Fluorescence images of PMMA coated on cover glass without and with $(Im)_3H^+$ deposition in special areas that resemble small circles. (E) Fluorescence spectra of $(Im)_3H^+$ clusters (black line) compared with TD-DFT calculations of the $(Im)_3H^+$ cluster (blue line). The input full-width at half maximum (FWHM) was set to 0.100 eV. (F) Fluorescence emission intensity of the $(Im)_3H^+$ clusters, changed with time under laser irradiation measured at different positions.

to the deexcitation of the S_1 to S_0 state of this cluster. It is inferred that the structure of the $(Im)_3H^+$ clusters is largely maintained in the soft-landing deposition process. The experimental observation of a broad band at 686 nm could be associated with molecular aggregation [58,59]. As a comparison, we also measured the emission of diluted solution of imidazole and simulated the fluorescence spectra of a single imidazole molecule of which the deexcitation of S_1 to S_0 state corresponds to emission at 351 nm (Figures S15 and S16), indicating significantly modulated emission of the $(Im)_3H^+$ clusters. It is worth noting the small half-peak width of the 516-nm emission (Figure 4E). Narrow-band luminophores are of well-known importance for their roles in critical fields such as information monitoring and photoelectric displays with high colour purity [60]. Low-dimensional nanomaterials of quantum dots and one-dimensional structures could give rise to fluorescence narrowing due to the quantum confinement effect, unique molecular states, and cross-linkers [61,62].

4 Conclusions

Utilizing a reflectron time-of-flight mass spectrometer, we studied the reactions of Cu^+ and Ag^+ with imidazole and 1-benzylimidazole. Metal complexes of $[M(Im)_{1-2}]^+$ and $[M(bim)_{1-2}]^+$ (M = Cu, Ag) and protonated imidazole clusters including $(Im)_{1-4}H^+$ and $(bim)_{1-2}H^+$ were efficiently produced under controllable conditions, showing tuneable reactivity of such organic molecules dominated by weak interactions. An interesting compound 1,3-dibenzylimidazole with a tuning-fork structure was also generated in this gas-phase reaction. Energetics and energy decomposition analyses, along with orbital and topological analyses, elucidated the chemical mechanism involved in the selectivity of formatting stable metal complexes and organic molecular clusters. DFT calculations illustrated the strong hydrogen-bond interactions in the $(Im)_{1-4}H^+$ and $(bim)_{1-2}H^+$ clusters. Furthermore, we achieved soft-landing deposition of Im_3H^+ on PMMA-coated cover glass and measured the fluorescence emission of such cluster quantum dots, showing narrow-width fluorescence at 516 nm. This is consistent with the TD-DFT calculation results. This study enriches the basic and precise properties of the heteroaromatic molecules in forming small molecular aggregates and complexes.

Acknowledgements We thank Prof. Hannu Häkkinen at the University of Jyväskylä for his friendly communication and discussion. This work was supported by the Ministry of Science and Technology of China (2020YFA0714602), the National Natural Science Foundation of China (92261113), and the CAS Key Research Program of Frontier Sciences (QYZDBSSW-SLH024).

Conflict of interest The authors declare no conflict of interest.

Supporting information The supporting information is available online at http://chem.scichina.com and http://link.springer.com/journal/11426. The supporting materials are published as submitted, without typesetting or editing. The responsibility for scientific accuracy and content remains entirely with the authors.

1 Dupont J, de Souza RF, Suarez PAZ. *Chem Rev*, 2002, 102: 3667–3692
2 Garrison JC, Youngs WJ. *Chem Rev*, 2005, 105: 3978–4008
3 Bureekaew S, Horike S, Higuchi M, Mizuno M, Kawamura T, Tanaka D, Yanai N, Kitagawa S. *Nat Mater*, 2009, 8: 831–836
4 Yang L, Liu Z, Neisiany RE, Lou J, Guo Y, Zhang L, Liu H, Chen S, Gu S, You Z. *Sci China Chem*, 2023, 66: 853–862
5 Wang J, Lin W, Li W. *Biomaterials*, 2013, 34: 7429–7436
6 Liu Y, Niu J, Wang W, Dong B, Lin W. *J Mater Chem B*, 2017, 5: 7801–7808
7 Sjöberg S. . *Pure Appl Chem*, 1997, 69: 1549–1570
8 Li Z, Song LF, Sharma G, Koca Fındık B, Merz Jr. KM. *J Chem Theor Comput*, 2022, 19: 619–625
9 Lee JC, Laydon JT, McDonnell PC, Gallagher TF, Kumar S, Green D, McNulty D, Blumenthal MJ, Keys JR, Land Vatter SW, Strickler JE, McLaughlin MM, Siemens IR, Fisher SM, Livi GP, White JR, Adams JL, Young PR. *Nature*, 1994, 372: 739–746
10 Jiang HY, Zhou CH, Luo K, Chen H, Lan JB, Xie RG. *J Mol Catal A-Chem*, 2006, 260: 288–294
11 Ali I, Lone MN, Aboul-Enein HY. *Med Chem Commun*, 2017, 8: 1742–1773
12 Poterya V, Tkáč O, Fedor J, Fárník M, Slavíček P, Buck U. *Int J Mass Spectrometry*, 2010, 290: 85–93
13 Wennberg PO, Bates KH, Crounse JD, Dodson LG, McVay RC, Mertens LA, Nguyen TB, Praske E, Schwantes RH, Smarte MD, St Clair JM, Teng AP, Zhang X, Seinfeld JH. *Chem Rev*, 2018, 118: 3337–3390
14 Luo Z, Castleman Jr. AW, Khanna SN. *Chem Rev*, 2016, 116: 14456–14492
15 Bromann K, Felix C, Brune H, Harbich W, Monot R, Buttet J, Kern K. *Science*, 1996, 274: 956–958
16 Miller SA, Luo H, Pachuta SJ, Cooks RG. *Science*, 1997, 275: 1447–1450
17 Ouyang Z, Takats Z, Blake TA, Gologan B, Guymon AJ, Wiseman JM, Oliver JC, Davisson VJ, Cooks RG. *Science*, 2003, 301: 1351–1354
18 Palmer RE, Pratontep S, Boyen HG. *Nat Mater*, 2003, 2: 443–448
19 Yoon B, Hakkinen H, Landman U, Worz AS, Antonietti JM, Abbet S, Judai K, Heiz U. *Science*, 2005, 307: 403–407
20 Esch F, Fabris S, Zhou L, Montini T, Africh C, Fornasiero P, Comelli G, Rosei R. *Science*, 2005, 309: 752–755
21 Antonietti JM, Gong J, Habibpour V, Röttgen MA, Abbet S, Harding CJ, Arenz M, Heiz U, Gerber C. *Rev Sci Instruments*, 2007, 78: 054101
22 Nagaoka S, Matsumoto T, Ikemoto K, Mitsui M, Nakajima A. *J Am Chem Soc*, 2007, 129: 1528–1529
23 Herzing AA, Kiely CJ, Carley AF, Landon P, Hutchings GJ. *Science*, 2008, 321: 1331–1335
24 Wang P, Laskin J. *Angew Chem Int Ed*, 2008, 47: 6678–6680
25 Lei Y, Mehmood F, Lee S, Greeley J, Lee B, Seifert S, Winans RE, Elam JW, Meyer RJ, Redfern PC, Teschner D, Schlögl R, Pellin MJ, Curtiss LA, Vajda S. *Science*, 2010, 328: 224–228
26 Nesselberger M, Roefzaad M, Fayçal Hamou R, Ulrich Biedermann P, Schweinberger FF, Kunz S, Schloegl K, Wiberg GKH, Ashton S, Heiz U, Mayrhofer KJJ, Arenz M. *Nat Mater*, 2013, 12: 919–924
27 Tsukamoto T, Haruta N, Kambe T, Kuzume A, Yamamoto K. *Nat Commun*, 2019, 10: 3727
28 Foster DM, Ferrando R, Palmer RE. *Nat Commun*, 2018, 9: 1323
29 Laskin J, Johnson GE, Warneke J, Prabhakaran V. *Angew Chem Int Ed*, 2018, 57: 16270–16284
30 Guo M, Yin B, Huang B, Wu H, Luo Z. *J Mater Chem C*, 2020, 8: 10325–10332
31 Frisch MJ, Trucks GW, Schlegel HB, et al. Gaussian 16 rev. B.01. Wallingford, CT: Gaussian, Inc., 2016
32 Stewart JJP. MOPAC 2016. Stewart Computational Chemistry, Colorado Springs, Colorado, USA, 2016, http://www.keinsci.com/research/molclus.html
33 Lu T. Molclus Program, Version 1.9.9.7. 2022, http://www.keinsci.com/research/molclus.html
34 Adamo C, Barone V. *J Chem Phys*, 1999, 110: 6158–6170
35 Glendening ED, Landis CR, Weinhold F. *J Comput Chem*, 2013, 34: 1429–1437
36 te Velde G, Bickelhaupt FM, Baerends EJ, Fonseca Guerra C, van Gisbergen SJA, Snijders JG, Ziegler T. *J Comput Chem*, 2001, 22: 931–967
37 Su P, Li H. *J Chem Phys*, 2009, 131: 014102
38 Baerends EJ, Ziegler T, Autschbach J, et al. ADF2018, scm. Amsterdam: Vrije Universiteit, 2018, http://www.scm.com
39 Zhang J, Lu T. *Phys Chem Chem Phys*, 2021, 23: 20323–20328
40 Lu T, Chen Q. *J Comput Chem*, 2022, 43: 539–555
41 Humphrey W, Dalke A, Schulten K. *J Mol Graphics*, 1996, 14: 33–38
42 Lu T, Chen F. *J Comput Chem*, 2012, 33: 580–592
43 Grimme S, Antony J, Ehrlich S, Krieg H. *J Chem Phys*, 2010, 132: 154104
44 Perdew JP, Yue W. *Phys Rev B*, 1986, 33: 8800–8802
45 Weigend F, Ahlrichs R. *Phys Chem Chem Phys*, 2005, 7: 3297–3305

46 Zhou M, Vdović S, Long S, Zhu M, Yan L, Wang Y, Niu Y, Wang X, Guo Q, Jin R, Xia A. *J Phys Chem A*, 2013, 117: 10294–10303
47 Gerardi HK, Gardenier GH, Viswanathan U, Auerbach SM, Johnson MA. *Chem Phys Lett*, 2011, 501: 172–178
48 Leclercq L, Schmitzer AR. *J Phys Chem A*, 2008, 112: 4996–5001
49 Reckziegel A, Kour M, Battistella B, Mebs S, Beuthert K, Berger R, Werncke CG. *Angew Chem Int Ed*, 2021, 60: 15376–15380
50 Wang X, Wang Y, Li P, Zhang X, Liu J, Hou Y, Zhang Y, Zhu Q, Han B. *ChemCatChem*, 2024, 16: e202401138
51 Chen D, Liu J, Shen J, Zhang Y, Shao H, Chen C, Wang S. *Adv Energy Mater*, 2024, 14: 2303820
52 Gross JH. *Mass Spectrometry*. 3rd Ed. Cham: Springer Nature, 2017. 968
53 Yoon B, Koskinen P, Huber B, Kostko O, von Issendorff B, Häkkinen H, Moseler M, Landman U. *ChemPhysChem*, 2007, 8: 157–161
54 Yang M, Wu H, Huang B, Luo Z. *J Phys Chem A*, 2019, 123: 6921–6926
55 Espinosa E, Alkorta I, Elguero J, Molins E. *J Chem Phys*, 2002, 117: 5529–5542
56 Guo M, Huang B, Yi Q, Luo Z. *Phys Chem Chem Phys*, 2021, 23: 16334–16340
57 Xie M, Liu H, Wan S, Lu X, Hong D, Du Y, Yang W, Wei Z, Fang S, Tao CL, Xu D, Wang B, Lu S, Wu XJ, Xu W, Orrit M, Tian Y. *Nat Commun*, 2022, 13: 3330
58 Yang T, Li Y, Zhao Z, Yuan WZ. *Sci China Chem*, 2022, 66: 367–387
59 Liu D, Zhao Z, Tang BZ. *Sci Sin-Chim*, 2022, 52: 1524–1546
60 Shi WQ, Zeng L, He RL, Han XS, Guan ZJ, Zhou M, Wang QM. *Science*, 2024, 383: 326–330
61 Zhao YS, Fu H, Peng A, Ma Y, Xiao D, Yao J. *Adv Mater*, 2008, 20: 2859–2876
62 Ai L, Yang Y, Wang B, Chang J, Tang Z, Yang B, Lu S. *Sci Bull*, 2021, 66: 839–856